J. Fluid Mech. (2019), *vol.* 878, *pp.* 481–501. © Cambridge University Press 2019
doi:10.1017/jfm.2019.618

Extreme long waves over a varying bathymetry

James G. Herterich[1,2,†] **and Frédéric Dias**[1,2,3]

[1]School of Mathematics and Statistics, University College Dublin, Dublin 4, Ireland

[2]Earth Institute, University College Dublin, Dublin 4, Ireland

[3]CMLA, ENS Paris–Saclay, CNRS, Université Paris–Saclay, 94235 Cachan, France

(Received 27 July 2018; revised 23 July 2019; accepted 26 July 2019;
first published online 17 September 2019)

Recent modelling work has shown that abrupt bathymetric transitions can produce dramatic amplifications of long waves, under the influence of both nonlinearity and dispersion. Here, the evolution of wave packets towards a vertical wall over a varying bathymetry is investigated with a one-dimensional conformal-mapping spectral code. In this system, wave breaking, runup and reflection, wave interference and bathymetric effects are highlighted. Wave breaking is examined with respect to geometric, kinematic and energetic conditions, with consistent results. The breaking strength is characterized for spilling and plunging based on initial wave period and amplitude. Non-breaking waves are amplified by reflection, interference and the bathymetry leading to large runups. In a typical example inspired by a real-world bathymetry, the maximum runup amplification approaches a factor of 12 – large enough for a 3 m amplitude wave to overtop a 30 m cliff.

Key words: surface gravity waves, wave breaking, wave–structure interactions

1. Introduction

The interaction of a breaking wave with a vertical wall can be dramatic, significantly increasing the water velocity, especially if the interaction occurs during the inception of overturning. Breaking-wave impact creates turbulence and pockets of trapped air, generating a water jet when the steep wave front impacts the wall (Cooker & Peregrine 1995; Peregrine 2003; Lugni, Brocchini & Faltinsen 2006; Dias & Ghidaglia 2018). Impact pressures increase with wave period (Goda 1975). If the vertical wall has a finite height, overtopping can occur. Non-breaking waves may lead to a surge overtopping with a fast bore developing from the collapsing surge (Hansom, Barltrop & Hall 2008). What is less known is the interaction of long waves with a vertical wall. In this paper, we consider runup amplification of long waves at arbitrarily high walls, without the overtopping that may occur with a finite wall (Ryu, Chang & Mercier 2007; Ryu & Chang 2008).

Runup amplification of shallow-water waves over a flat bathymetry can be significantly larger than that given by linear theory (factor of 5–6 as opposed to 2) due to a combination of reflection, constructive interference, dispersion and other nonlinear effects (Carbone *et al.* 2013; Viotti, Carbone & Dias 2014*a*; Akrish

†Email address for correspondence: james.herterich@ucd.ie

https://doi.org/10.1017/jfm.2019.618 Published online by Cambridge University Press

et al. 2016*b*). Head-on solitary wave collisions produce large runup jets (Chambarel, Kharif & Touboul 2009; Chen *et al.* 2015). Long wave packets usually disintegrate into a bore formation with smaller wavelengths (Akrish, Rabinovitch & Agnon 2016*a*; Akrish *et al.* 2016*b*; Brühl & Oumeraci 2016; Trillo *et al.* 2016; Ning, Li & Zhang 2018). Large runup amplifications are supported by higher frequencies in the spectrum. The resulting nonlinear interactions increase dynamic pressure, but reduce the peak force compared to linear theory. However, that force acts for a longer duration when multiple peaks develop (Brennan, Viotti & Dias 2014; Akrish *et al.* 2016*b*). Interestingly, a varying bathymetry that becomes shallower closer to the wall further reduces the force during runup, as compared to the flat case, even though the amplification is greater (Brennan *et al.* 2017).

The influence of bathymetry on wave conditions is evident. In numerical simulations over a flat bathymetry, small-amplitude long waves do not exhibit breaking during runup at a wall. However, once a variable bathymetry is introduced, steep wave fronts develop. Furthermore, strong variations in depth enhance the amplification of waves (Viotti & Dias 2014; Bolles, Speer & Moore 2019). Waves can break, for example through the overturning of the wave crest. The onset of wave breaking is typically characterized by a steep asymmetric wave and the formation of whitewater (due to entrained air from turbulence) at the crest tip that falls down the face of the wave (Banner *et al.* 2014; Kurnia & van Groesen 2017). Wave breaking adds vorticity, turbulence and heat diffusion to the system (Longo *et al.* 2017).

The physics of a breaking wave leads to several different criteria for determining the onset of wave breaking: geometric (Hwang, Xu & Wu 1989; Wu & Nepf 2002; Perlin, Choi & Tian 2013; Grue, Kolaas & Jensen 2014), kinematic (Hwang *et al.* 1989; Stansell & MacFarlane 2002; Wu & Nepf 2002; Perlin *et al.* 2013) and energetic (Perlin *et al.* 2013; Seiffert, Ducrozet & Bonnefoy 2017; Barthelemy *et al.* 2018; Seiffert & Ducrozet 2018). These criteria are evaluated locally, as the extremal conditions for wave breaking may not be seen in global wave-parameter values. Wind forcing alters these conditions as it enhances wave steepness. However, this is only significant for strong winds acting over long scales (Babanin *et al.* 2010). Wave breaking depends on the shape and/or motion of the free surface, which is altered by the wind (Hwang *et al.* 1989). Wind may act to delay the onset of breaking by supporting steeper waves (Iafrati, De Vita & Verzicco 2019), yet increase the frequency of breaking waves as the wind velocity increases (Xu, Hwang & Wu 1986). Dynamic criteria only change by a few percent as wind forcing and spectral bandwidth change (Saket *et al.* 2017, 2018).

In this paper, we analyse the fundamental problem of long wave groups propagating towards vertical walls. We only determine the onset of wave breaking, as the numerical code for the Euler equations used cannot resolve beyond the breaking process. The breaking strength is strongly related to the onset of breaking (Derakhti, Banner & Kirby 2018). From this we may infer the wave behaviour in the zone where broken waves are present, such as whitecapping and plunging (Phillips 1985; Drazen, Melville & Lenain 2008), without necessarily computing the flow. We consider the runup of a wave packet at a vertical wall over a simplified variable bathymetry, chosen as representative of the Aran Islands, Ireland. We briefly summarize preliminary results, presented at recent conferences, on wave breaking and runup. Furthermore, we consider additional and new measures of wave breaking and breaking strength. For non-breaking waves, nonlinear interactions among waves, vertical wall and bathymetry result in a maximum runup amplification that approaches a factor of 12 – large enough for a 3 m amplitude wave to overtop a 30 m cliff. Finally, we discuss the relevance of our results to the real world.

https://doi.org/10.1017/jfm.2019.618 Published online by Cambridge University Press

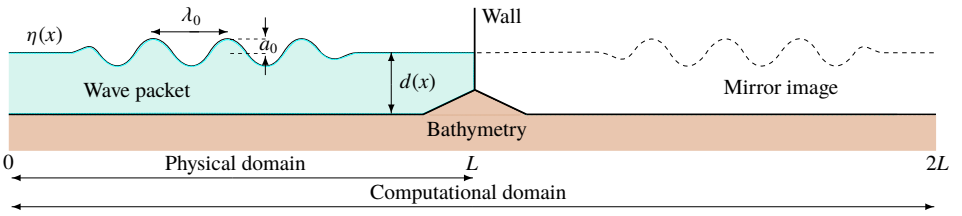


FIGURE 1. (Colour online) Sketch of model set-up with incoming wave packet $\eta(x)$ approaching a vertical wall over a variable bathymetry profile relative to the still-water depth $d(x)$. The bathymetry is horizontal away from the wall, becoming shallower closer to shore. The waves have initial amplitude a_0 and wavelength λ_0. There are N_w waves (crests and troughs) in each wave packet. The numerical method constructs a mirror image to simulate a vertical wall.

2. Model

2.1. *Set-up*

We consider the runup of a packet of long waves approaching a vertical wall over a variable bathymetry, with bathymetry profile given relative to the still-water depth $d(x)$. A sketch of the set-up is shown in figure 1. We describe the wave packet's motion by the incompressible Euler equations,

$$\nabla^2\Phi = 0, \quad 0 < x < 2L, \quad -d(x) < y < \eta(x,t), \tag{2.1}$$

$$\eta_t = -\Phi_x\eta_x + \Phi_y, \quad 0 < x < 2L, \quad y = \eta(x,t), \tag{2.2}$$

$$\Phi_t = -\tfrac{1}{2}(\Phi_x^2 + \Phi_y^2) - g\eta, \quad 0 < x < 2L, \quad y = \eta(x,t), \tag{2.3}$$

$$\Phi_x d_x + \Phi_y = 0, \quad 0 < x < 2L, \quad y = -d(x), \tag{2.4}$$

where $\eta(x,\,t)$ is the free surface, $\Phi(x,\,y,\,t)$ is the velocity potential and g is the acceleration due to gravity (Brennan *et al.* 2017). Note that the water depth $d(x) > 0$, with $y = 0$ the still-water level. The constant water depth far upstream where the bathymetry is flat is denoted by h. We solve (2.1) with a conformal-mapping spectral method (Choi & Camassa 1999), using a mirror wave image to impose the wall boundary condition at $x = L$ and for periodicity (Viotti *et al.* 2014*a*). Hence, $0 < x < L$ is the physical domain and $0 < x < 2L$ is the computational domain, with periodic boundary conditions imposed at $x = 0,\ 2L$ (figure 1). The incoming wave packet experiences runup amplification, R, at the vertical wall, given by

$$R(t) = \frac{\eta(x = L,\,t)}{a_0}, \tag{2.5}$$

where a_0 is the initial amplitude of the incoming wave packet.

The waves we consider can be easily reproduced in laboratory experiments (Brühl & Oumeraci 2016; Trillo *et al.* 2016). Their relevance to the real world is discussed in § 5. We use a bathymetry inspired by that of the Aran Islands off the west coast of Ireland. In figure 2 we show three transects (dimensionless, scaled by $h = 80$ m) taken with INSS and INFOMAR data from Geological Survey Ireland (2002–2016). We observe that the slope near the coast is an order of magnitude greater than that farther out. To represent this bathymetry, we approximate these data (dashed line in figure 2) as a piecewise-continuous linear function with a slope of 0.01 for the first 4 km from

https://doi.org/10.1017/jfm.2019.618 Published online by Cambridge University Press

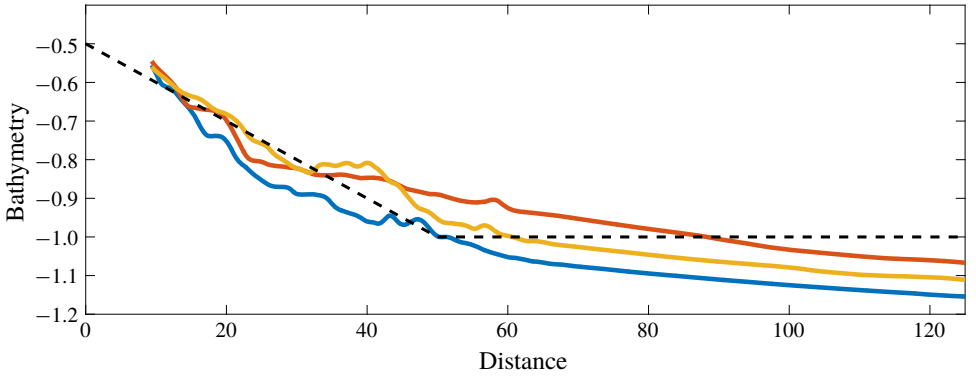


FIGURE 2. (Colour online) Three bathymetry transects (solid curves) perpendicularly to the western-side cliffs of Inis Mór. Image created from INSS and INFOMAR data from Geological Survey Ireland (2002–2016). The dashed line represents the idealized piecewise continuous representation of the bathymetry. The data are non-dimensionalized with respect to the typical depth, $h = 80$ m. Hence a 40 m ($= |-0.5| \times 80$ m) depth at the cliff face and a flat bathymetry from 4 km ($= 50 \times 80$ m). For a laboratory experiment at scale 1/100, the depth would be 40 cm at the wall and the flat bathymetry (80 cm) would start at 40 m from the wall.

the coast, followed by a constant value. Considering an effective composite slope for the seabed is typical in the literature (Saville Jr 1957; Mayer & Kriebel 1995). As bathymetry data are not available for closer than 750 m from the shoreline, we have extrapolated the bathymetry profile for our simplified approximation in this area. The depth at the cliffs is approximately 40 m and the ocean depth is approximately 80 m. Note that there is a tidal change of 5 m in this area. We address the effect of tidal differences by changing the location of the free surface, but keeping the bathymetry the same. We neglect the presence of any current.

From now on, all lengths are scaled with the constant ocean depth, $h = 80$ m, and time with $\tau = (h/g)^{1/2} \approx 2.859$ s. A laboratory replica of this situation at scale 1/100 (water depth of 80 cm) would produce wave parameters (amplitude, period, water depth) quite similar to the values found in Brühl & Oumeraci (2016) and in Trillo *et al.* (2016).

We model an initial incoming wave packet, traversing from flat to non-flat bathymetry leading to the vertical wall (figure 1). The wave packet is well defined away from the wall, characterized by the following independent parameters: the number of waves N_w, the initial amplitude a_0 and the period P_0. Other parameters (angular frequency ω_0, wavenumber k_0 and wavelength λ_0) are related via common wave relations such as the dispersion relation. The initialized wave packet, $\eta_0(x) = \eta(x, t = 0)$ and $\Phi_0(x) = \Phi(x, t = 0)$, is a sinusoidal group modulated by a hyperbolic tangent function (Viotti *et al.* 2014*a*),

$$\eta_0(x) = a_0 \cos[k_0(x - x_0)]M(x) + \text{image}, \tag{2.6}$$

$$\Phi_0(x) = a_0 c(x) \coth[k_0 d(x)] \sin[k_0(x - x_0)]M(x) + \text{image}, \tag{2.7}$$

where $M(x) = 1/2[\tanh((x - x_0)/\delta) - \tanh((x - x_0 - N_w\lambda_0)/\delta)]$ is a modulating function and $c(x) = [g \tanh(k_0 d(x))/k_0]^{1/2}$ is a phase velocity. The subscript 0 refers to initial reference values and $\delta = \lambda_0/6$ is a fitting factor. The runup of long-period cosine

https://doi.org/10.1017/jfm.2019.618 Published online by Cambridge University Press

Parameter	Symbol	Real world	Laboratory	Dimensionless
Period	P_0	50–900 s	5–90 s	17.5–315
Amplitude	a_0	1–8 m	1–8 cm	0.0125–0.1
Number of waves	N_w	N/A	N/A	1–6
*Frequency	ω_0	0.007–0.126 s^{-1}	0.07–1.26 s^{-1}	0.02–0.36
*Wavenumber	k_0	0.00025–0.0046 m^{-1}	0.025–0.46 m^{-1}	0.02–0.37
*Wavelength	λ_0	1.37–25.2 km	13.7–252 m	17.1–315

TABLE 1. Parameter ranges for initial incoming wave packet. An asterisk signifies that the parameter is not independent but based on standard relations with the other parameters. The laboratory values are based on a 1/100 scale.

waves in shallow water has been the subject of experiments to understand the complex phenomena of near-shore dispersive breaking of long waves (Brühl & Oumeraci 2016; Trillo *et al.* 2016).

A summary of the wave parameter range is given in table 1. Note that the same symbol is used for dimensional and dimensionless variables. When there is ambiguity below, we specify whether it is the dimensional or the dimensionless value that is used. Since the combined parameter ranges could be reproduced in laboratory experiments, we simulate the full range, finding that large-amplitude long waves break up into wave trains as expected, and that those of the highest amplitudes always exhibit wave breaking. Though largely a theoretical exercise in these cases, we will see that it is the intermediate amplitude ranges of these high-amplitude wave packets that do not exhibit wave breaking and result in the highest runup amplifications. In the open ocean, tsunami waves can have wavelengths of 200 km and amplitude of 1 m in a depth of 4 km (Mader 1974; Mei, Stiassnie & Yue 1989; Craig 2006; Madsen, Fuhrman & Schäffer 2008). We initialize our wave packet with long waves that have already developed to higher amplitudes (table 1) near the coast and propagate towards the coast where disintegration typically occurs (Madsen *et al.* 2008). The initial wave packet of a modulated sinusoidal group evolves via a process of (i) steepening, (ii) undular bore formation and (iii) disintegration into solitons (Akrish *et al.* 2016*a*,*b*; Brühl & Oumeraci 2016; Trillo *et al.* 2016). The runup of such waves on a wall over a flat bathymetry has been characterized in the literature (Viotti *et al.* 2014*a*; Akrish *et al.* 2016*a*). Wave breaking is typically not observed for small amplitudes. The runup amplifications can be greater than six times the initial amplitude (Viotti *et al.* 2014*a*).

2.2. *Wave-breaking measures*

Breaking waves are measured by a number of criteria, including geometry, kinematics and energy, following the characterizing overturning process. During the onset of wave breaking, the wave form may break down, e.g. whitecapping, spilling, plunging, with local steep crests and reduced phase speed, before overturning fully occurs (Schwendeman & Thomson 2017). These processes are often reflected in practical criteria values; values that are lower than theoretical values. Furthermore, these are local events that are not always captured by global wave-parameter values. As such, local parameters are considered. In this section we describe some old and new wave-breaking criteria.

https://doi.org/10.1017/jfm.2019.618 Published online by Cambridge University Press

2.2.1. *Geometric*

The shape of the wave is an indicator for wave breaking, with many geometric metrics in use. These include crest front steepness, crest rear steepness, vertical and horizontal asymmetry factors (Wu & Tian 2000; Wu & Nepf 2002; Perlin *et al.* 2013). Many critical values for each of these metrics have been proposed, beyond which breaking occurs. We consider the following metric for wave steepness:

$$S = ka, \tag{2.8}$$

measured locally at the crest tip. A typical critical value is $S_{crit} \approx 0.43$ (Melville 1996; Wu & Nepf 2002; Toffoli *et al.* 2010). The type of breaking wave (spilling, plunging) is related to the magnitude of S, with steeper breaking waves more likely to be plunging than spilling (Perlin *et al.* 2013). However, geometric criteria such as steepness have been criticized in the literature for their inconsistency (Barthelemy *et al.* 2018). Non-breaking waves frequently attain steepness values that exceed those for breaking waves.

Ocean waves at finite depth are also measured with another geometric criterion, the ratio of wave height, H_w, to depth, d,

$$H = \frac{H_w}{d}. \tag{2.9}$$

Experimentally, the critical value for a horizontal seabed is $H_{crit} \approx 0.55$ (Riedel & Byrne 1987; Nelson 1994; Grue *et al.* 2014; Grue & Kolaas 2017; Saket *et al.* 2018). Other studies (Cyril & Galvin 1972; Grilli, Svendsen & Subramanya 1997) suggest higher values, particularly for solitary waves; however, including higher-order approximations of the Stokes and cnoidal theories reduces them to at most the experimental critical value (Massel 1996).

In the case of a seabed with a horizontal section followed by a slope, larger critical height-to-depth values (2.9) have been shown for random waves (Riedel & Byrne 1987) and solitary waves (Munk 1949; Grilli *et al.* 1997). This depends on wave characteristics such as initial shape, breaking steepness, nonlinearities, bottom friction and the degree of the seabed slope (Munk 1949; Goda 1975). However, these bathymetry profiles form a beach. Beaches with larger slopes (such as 1 : 8) permit high values of $H > 1$ (Munk 1949; Saville Jr 1957; Weggel 1973), whereas lower gradient beaches (such as 1 : 100) retain the condition $H < 0.55$ (Riedel & Byrne 1987). Furthermore, the critical H decreases with depth-to-wavelength ratio, so that shorter-period waves have smaller breaking heights. Many empirically derived functional formulae for H, incorporating beach slope and wavelength, have been proposed (Goda 1975, 2010).

In our case waves propagate over a slope of 1 : 100 until they reach a vertical wall (figures 1 and 2). Wave interaction with the wall can occur without wave breaking, resulting in incoming and reflecting wave–wave interactions that significantly amplify subsequent waves. This bathymetry-induced amplification is implicit in the steepness (2.8), but explicit in the wave height-to-depth ratio (2.9).

2.2.2. *Kinematic*

Physically, wave breaking occurs if the local fluid particle velocity, $|\boldsymbol{U}|$, exceeds the local wave phase velocity, C. The kinematic breaking measure is the ratio

$$K = \frac{|\boldsymbol{U}|}{C}, \tag{2.10}$$

https://doi.org/10.1017/jfm.2019.618 Published online by Cambridge University Press

with theoretical breaking condition $K_{crit} \geqslant 1$. Studies estimate the kinematic criterion (2.10) to be lower than 1 due to the onset of breaking (Wu & Nepf 2002; Kurnia & van Groesen 2017; Barthelemy *et al.* 2018). For practical reasons, such as the inability to resolve wave evolution after the onset of breaking, the criterion (2.10) may be taken to be as low as $K_{crit} \geqslant 0.7$ (Wu & Nepf 2002; Perlin *et al.* 2013). The type of breaking wave (spilling, plunging) is related to the magnitude of K, with $K_{crit}^{plunging} > K_{crit}^{spilling}$. However, the exact values are not well defined (Perlin *et al.* 2013). We consider critical values as defined by Wu & Nepf (2002) as we compute velocities based on their formulation. They suggest spilling occurs for $K > 1$ and plunging for $K > 1.5$.

The fluid velocity, $|\boldsymbol{U}|$, is derived from the local velocity field, $\boldsymbol{u} = (u, v)$,

$$|\boldsymbol{U}| = (u^2 + v^2)^{1/2} = (\Phi_x^2 + \Phi_y^2)^{1/2}. \tag{2.11}$$

The phase velocity, C, is given by the local wave parameters of angular frequency, ω, and wavenumber, k,

$$C = \frac{\omega}{|k|} = \left(\frac{g \tanh(kd)}{k}\right)^{1/2}, \tag{2.12}$$

via the dispersion relation $\omega^2 = gk \tanh(kd)$, for depth d. For our study, $d = d(x)$ is spatially varying (figure 2). The local wavenumber, k, takes the form of the gradient of the phase, given by

$$k = \frac{\eta\zeta_x - \eta_x\zeta}{\eta^2 + \zeta^2}, \tag{2.13}$$

where ζ is the conjugate to the free surface (Stansell & MacFarlane 2002; Kurnia & van Groesen 2014).

An alternative method is to first calculate the local angular frequency ω, with the wavenumber k given by the dispersion relation (Stansell & MacFarlane 2002; Wu & Nepf 2002; Kurnia & van Groesen 2014).

2.2.3. *Energetic*

A new energy breaking criterion has been proposed by Barthelemy *et al.* (2018). The criterion is based on the local normalized energy flux for deep and intermediate water depths, evaluated at the crest tip of a wave. The concept is that the wave cannot accommodate a local energy flux beyond that in the corresponding maximum recurrent case. Let p denote the pressure relative to the atmospheric pressure. The criterion is a ratio, B, between the local energy flux, $\boldsymbol{F} = \boldsymbol{u}(p + y + \frac{1}{2}||\boldsymbol{u}||^2)$, and the local energy density, $E = y + \frac{1}{2}||\boldsymbol{u}||^2$, given by

$$B = \frac{||\boldsymbol{F}||}{E|c|}, \tag{2.14}$$

where $c = -\eta_{xt}/\eta_{xx}$ is the crest speed (Fedele 2014). The crest speed arises from following the evolution of the crest tip $x_c(t)$, formally given by $c = \mathrm{d}x_c/\mathrm{d}t$ (Stansell & MacFarlane 2002). It is found that, for a flat bottom with deep to intermediate depth, the criterion for the onset of breaking is $0.85 < B_{crit} < 0.86$ (Barthelemy *et al.* 2018). This threshold increases by only a few percent as wind forcing becomes significant, decreases by a few percent as the spectral bandwidth increases and is unaffected by wavelength (Saket *et al.* 2017, 2018). At the free surface, $z = \eta$, where $p = 0$, the flux breaking metric (2.14) reduces to $B = |\boldsymbol{U}|/|c|$. This is a similar measure to the

https://doi.org/10.1017/jfm.2019.618 Published online by Cambridge University Press

kinematic criterion (2.10); however a dynamic leaning cycle during propagation results in a crest slowdown. This slowdown is observed by a probability density function centred at about 80 % of the phase speed (Banner *et al.* 2014; Fedele 2014).

The results in Barthelemy *et al.* (2018) are computed for waves that have reached, and are propagating at, their maximum height, so that no vertical component exists. During reflection of the wave at the vertical wall, however, $c \to 0$ as the crest changes direction, while $|\boldsymbol{U}| \not\to 0$ during runup due to the vertical velocity component. Hence, $B \to \infty$ during the period of most interest. For this reason, we do not explicitly calculate B. Instead, we use the above observation of its relation to the phase speed ($c \approx 0.8C$) to write

$$B \approx \frac{5}{4}\frac{|\boldsymbol{U}|}{C} = \frac{5}{4}K. \tag{2.15}$$

The range $0.85 < B_{crit} < 0.86$ is close to $\frac{5}{4}K_{crit} \approx 0.875$.

2.2.4. *Breaking strength*

After a wave breaks, energy is dissipated (Duncan 1983). This leads to a dimensionless measure of the breaking strength b,

$$b = \frac{g\tilde{\epsilon}}{\tau_b l \rho c_b^5}, \tag{2.16}$$

given in terms of the total energy dissipation $\tilde{\epsilon}$, fluid density ρ and characteristic scales of a breaking wave such as active breaking period τ_b, mean length l of the breaking crest and phase speed c_b of the breaking wave (Phillips 1985; Drazen *et al.* 2008).

Computing the total energy dissipation $\tilde{\epsilon}$ of an isolated breaking event requires simulating the event beyond the breaking point. However, Derakhti *et al.* (2018) show that the breaking strength is related to the rate of change of the normalized energy flux parameter B (2.14),

$$b = b\left(\frac{\mathrm{d}B}{\mathrm{d}t}\right). \tag{2.17}$$

The breaking strength increases with $\mathrm{d}B/\mathrm{d}t$. It is observed numerically that as B approaches its critical breaking value, the type of breaking depends on its rate of change. Plunging occurs for larger values of $\mathrm{d}B/\mathrm{d}t$ than spilling (Derakhti *et al.* 2018). We will compute $\mathrm{d}B/\mathrm{d}t$ during the onset of breaking and use it to characterize the breaking strength of long-wave wave packets.

3. Numerical methodology

We solve the Euler equations (2.1)–(2.4) with initial conditions (2.6) and (2.7) numerically, using a spectral conformal-mapping method. For a dimensionless system, the maximum depth is 1, and we take $g = 1$ (Viotti, Dutykh & Dias 2014*b*).

The spectral conformal-mapping method maps the problem from the physical domain of a propagating wave over a spatially varying bathymetry to a finite strip (Choi & Camassa 1999; Viotti *et al.* 2014*a*,*b*). The simulation is run with $N = 16\,384$ Fourier modes, with half the spectrum dealiased, giving suitable convergence (Brennan *et al.* 2017). Runup amplification at a vertical wall over a varying bathymetry compares well with other codes (Benoit *et al.* 2018). The physical domain (half the computational domain due to the mirror image) is $L = 50 + (2 + N_w)\lambda_0$ where 50

https://doi.org/10.1017/jfm.2019.618 Published online by Cambridge University Press

is the dimensionless length of the sloped region of the bathymetry (figure 2). The wave packet is initiated with its leading edge $1.5\lambda_0$ from the sloped region of the bathymetry (figure 1). The run time varies with each wave packet, allowing enough time for the waves to reach the vertical wall and fully reflect.

The initial wave packet (2.6) is not an exact solution of the problem, leading to a small transient adjustment. Furthermore, this imposed initial condition allows for the development of the undular bore and disintegration into solitons (Akrish *et al.* 2016*a*,*b*; Brühl & Oumeraci 2016; Trillo *et al.* 2016).

Solving the Euler equations (2.1)–(2.4) yields the time and space evolution of the free surface, $\eta(x, t)$, and the velocity potential, $\Phi(x, y, t)$. The crests and troughs are easily identified, with the amplitude a given by the crest height. The conjugate to the free surface, ζ, is calculated via a partial Hilbert transform with respect to x,

$$\zeta(x, t) = \mathcal{H}[\eta] = \frac{1}{\pi}\,\text{p.v.}\int_{-\infty}^{\infty} \frac{\eta(\chi, t)}{x - \chi}\,\mathrm{d}\chi, \tag{3.1}$$

where p.v. indicates the principal value of the integral (Stansell & MacFarlane 2002). This integral is a convolution of η and $1/\pi x$. As such, the computation may be greatly simplified using the convolution theorem, such that

$$\mathcal{F}[\mathcal{H}[\eta]](\nu) = -\mathrm{i}\,\mathrm{sgn}(\nu)\mathcal{F}[\eta](\nu), \tag{3.2}$$

since $\mathcal{F}[1/\pi x](\nu) = -\mathrm{i}\,\mathrm{sgn}(\nu)$. As a spectral method is used to solve the Euler equations (2.1)–(2.4), the Fourier transform of the free surface is computed, producing the Fourier coefficients in the conformal space. When calculating spatial derivatives, the chain rule and Cauchy–Riemann equations are used to appropriately calculate derivatives in physical space. Note that in the above calculations, the Fourier and Hilbert transforms are computed with respect to their discrete forms at each time step.

The breaking criteria are all computed with regard to local parameter values. We only consider those values at the crest tips. Whereas some studies (Barthelemy *et al.* 2018) consider only the crest tips at the highest attained elevation, with no vertical velocity component, we follow the crest tips throughout their evolution. This is necessary as the varying bathymetry significantly influences the amplitude throughout its evolution. However, we restrict (filter) consideration of certain crests via two conditions: (i) crests that are at least 10 % larger in amplitude than nearby crests, (ii) crests with amplitudes that are at least 50 % the initial amplitude. The first condition filters the smaller-amplitude crests on a wave train. The second condition filters waves with near-zero surface displacement that result in an artificial blowup of the criteria.

The wave height, H_w, is calculated at the crest peaks throughout the evolution of the wave packet. We determine H_w based on the trough in front of each crest. That is, we consider the direction (towards or away from the vertical wall) in which each crest is travelling and use the trough ahead of it. We determine the direction of the wave by the sign of the horizontal velocity component.

The runup amplification is only considered for non-breaking waves. Since we cannot solve for the wave evolution beyond breaking (Viotti *et al.* 2014*a*), we do not know the full extent of runup amplification. This is highlighted by studies suggesting that the runup of breaking waves may contain water jets due to high pressures and trapped air (Peregrine 2003).

Finally, in the case of breaking waves, we compute the criteria during the onset of breaking at finer ($\times 100$) time intervals than throughout the simulation. This provides a more accurate measure for critical values. The breaking strength parameter (2.17) is computed with a simple finite-difference discretization.

https://doi.org/10.1017/jfm.2019.618 Published online by Cambridge University Press

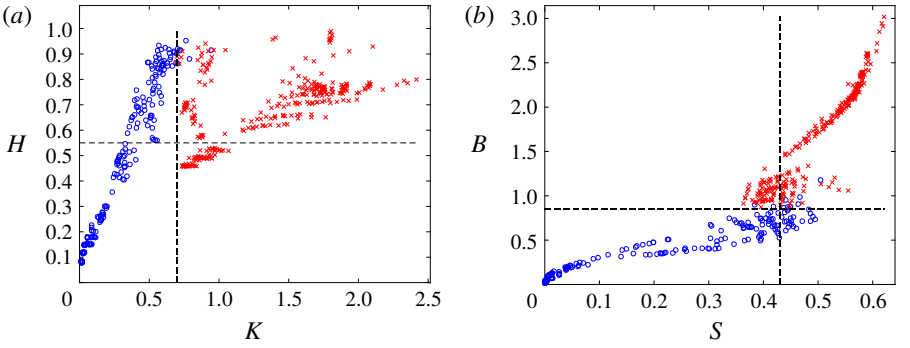


FIGURE 3. (Colour online) Comparison of steepness S (2.8), wave height-to-depth ratio H (2.9), kinematic K (2.10), and energetic B (2.15) wave-breaking measures. We distinguish between non-breaking (○) and breaking (×) waves. Each marker represents a simulation with initial conditions from table 1. (*a*) Height-to-depth ratio and kinematic. (*b*) Energetic and steepness. The dashed lines are accepted critical values.

4. Results

4.1. *Wave evolution*

We solve the Euler equations (2.1)–(2.4) for the free surface η and velocity potential Φ, with initial conditions (2.6) and (2.7) taking parameter values in table 1. Typically, the large amplifications of crests occur during wave–wave and wave–wall interactions, with bathymetry playing a significant role. The wave packet breaks up into a wave train near the wall (Herterich & Dias 2017*a*), as expected from long waves propagating towards a shore (Madsen & Fuhrman 2008; Madsen *et al.* 2008; Brühl & Oumeraci 2016; Trillo *et al.* 2016).

We begin by examining wave breaking during wave evolution. We quantify the process by the various criteria as discussed in § 2.2, and treat breaking and non-breaking waves differently. We determine a measure of the breaking strength (2.17). For non-breaking waves, we measure the runup amplification R (2.5), a local measure of wave interaction with a wall and consider extreme waves that reach the wall.

4.2. *Wave breaking*

4.2.1. *Summary of preliminary results*

The evolution of wave packets, as described, often results in a breakdown of the numerical solver. We establish that this is a result of the physical phenomenon of wave breaking. As this is not captured in our model, the solver cannot resolve the wave form.

We simulate wave packets with initial conditions from table 1, especially parameter values about where the waves appear to transition from non-breaking to breaking. The waves with greatest steepness S (2.8), wave height-to-depth ratio H (2.9), kinematic K (2.10), and, by inference, energetic B (2.15) measures are determined for each simulation. Comparisons of the different measures are shown in figure 3, with more simulations performed than reported in Herterich & Dias (2017*a*,*b*).

As discussed, there is often inconsistency in both geometric measures; non-breaking waves which exceed typical criteria values, and *vice versa*, as often reported. The critical ranges are summarized in table 2. There are many non-breaking waves that

https://doi.org/10.1017/jfm.2019.618 Published online by Cambridge University Press

Criteria	Max non-breaking	Min breaking	Accepted criteria
S	0.504	0.364	$\approx$0.43
H	0.951	0.452	$\approx$0.55
K	0.944	0.697	$\geqslant$0.7
B	1.18	0.871	$\approx$0.86

TABLE 2. Geometric criteria S (2.8) and H (2.9), kinematic criteria K (2.10) and energetic criteria B (2.15), for wave breaking of simulated wave packets approaching a wall (figures 1 and 2). The initial parameter values are from the ranges given in table 1.

significantly exceed the critical values. However, in the kinematic case, the maximum (0.951) is still below the theoretical critical value of 1. We will analyse these waves in more detail in the subsequent sections of the paper. However, the lower bounds for breaking by the kinematic and energetic measures are consistent with the literature (Wu & Nepf 2002; Barthelemy *et al.* 2018).

There is a clear linear trend in the relationships among geometric (S and H), kinematic (K) and energetic (B) measures for non-breaking waves. The kinematic and energetic measures best adhere to the accepted criteria. The dimensionless amplitude a_0 and number of waves N_w are the biggest factors related to wave breaking, as discussed in Herterich & Dias (2017*a*). These influence the wave–wave interactions that amplify and steepen waves, similar to the flat case (Carbone *et al.* 2013). For example, the amplitude above which breaking usually occurs can be up to 50 % higher for $N_w = 1$ (dimensionless amplitude $a_0 > 0.063$) than $N_w > 1$ (dimensionless amplitude $a_0 > 0.043$).

4.2.2. *Breaking strength*

The breaking strength is related to the onset of breaking via the energetic measure B (2.15), as discussed in § 2.2.4. The breaking strength parameter also takes the form $b = b(\mathrm{d}B/\mathrm{d}t)$ (2.17). We observe the quantity $\mathrm{d}B/\mathrm{d}t$ to increase with B (figure 4). As B is a measure of energy flux, we expect more energetic fluxes to have larger breaking strengths. The values of $\mathrm{d}B/\mathrm{d}t$ obtained are of similar order of magnitude to the $\Gamma \propto \mathrm{d}B/\mathrm{d}t$ in figure 5 of Derakhti *et al.* (2018). Note that we neglect the scaling in the proportionality for Γ as our simulations are already dimensionless.

Classifying the initial waves that correspond to each simulation in figures 3 and 4 is relatively simple. In general, all measures S, H, K, B and $\mathrm{d}B/\mathrm{d}t$ increase with initial amplitude a_0 and decrease with period P_0, as expected. This is in agreement with experiments (Goda 1975, 2010). The initial wave profile has an effect on the final breaking strength. Waves with greater initial amplitudes are more likely to result in plunging (figure 4*b*). However, for wave periods it is less clear (figure 4*c*). There are similar numbers of waves that exhibit plunging as well as spilling for all initial wave periods. Note that many long waves break up into wave trains with smaller periods.

4.3. *Runup amplification*

4.3.1. *Summary of preliminary results*

Each wave in the wave packet is amplified at the wall. However, we consider a single parameter to represent the runup in each simulation (from table 1), the maximum runup amplification,

$$R_{max} = \max(R(t)). \tag{4.1}$$

https://doi.org/10.1017/jfm.2019.618 Published online by Cambridge University Press

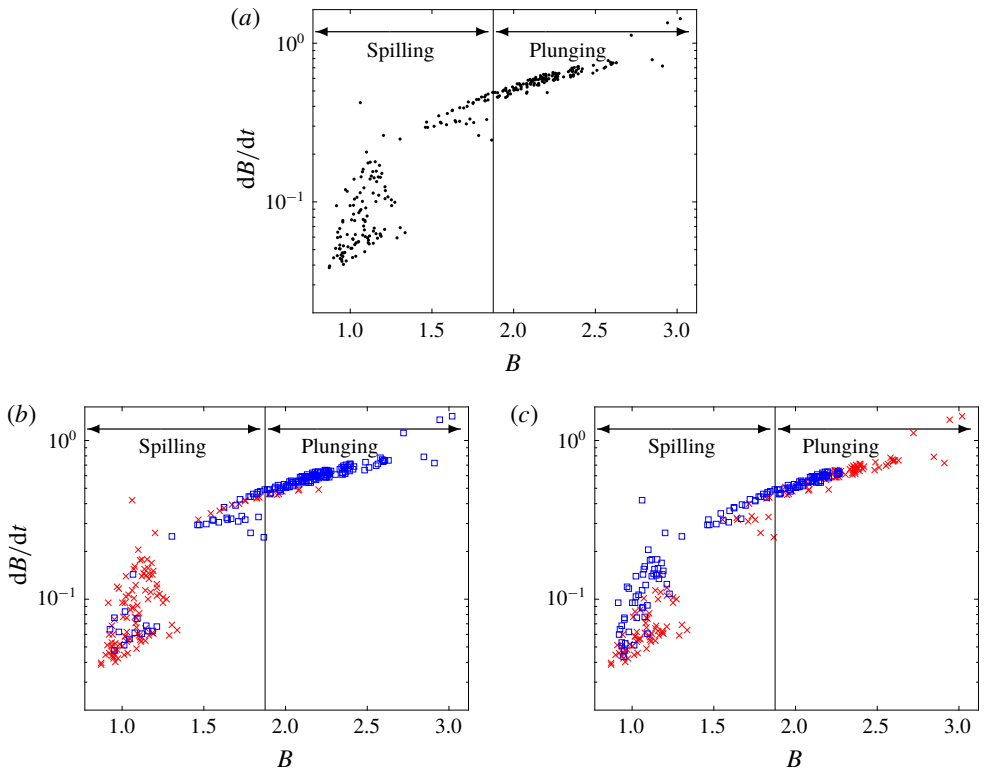


FIGURE 4. (Colour online) (*a*) The rate of change of B (2.15) for breaking waves, an indicator of the breaking strength for all waves. In (*b*,*c*) we group the results in (*a*) with respect to initial wave amplitude and period: (*b*) $0.04 < a_0 < 0.06$ (×) and $0.06 < a_0 < 0.1$ (□); (*c*) $P_0 < 210$ (×) and $210 < P_0 < 315$ (□). The ranges for the types of breaking (spilling and plunging) are from Wu & Nepf (2002), converted from a condition on K to B, via (2.15).

In general, R_{max} increases with the amplitude of the initial wave packet. As we do not know the subsequent wave evolution for breaking waves, after the onset of breaking, we do not consider these waves here. Typically, waves break for $a_0 > 0.04$ (Herterich & Dias 2017*a*). The runup amplification steadies out with respect to N_w for $N_w \geqslant 3$, as for a flat bathymetry (Viotti *et al.* 2014*a*).

Increasing the bathymetry slope (figure 1) from flat to 1 % almost doubles the runup amplification, with $R_{max} > 10$ in all cases. Dimensionally, this means that a wave packet of initial amplitude 3 m can overtop a 30 m cliff in ocean-type conditions. In the laboratory, that would correspond to a 3 cm wave overtopping a 30 cm cliff.

4.3.2. *Tidal effects*

The tide affects the absolute depth over a bathymetry profile. While the bathymetry clearly is important in runup amplification, changes in the tide can increase or decrease its influence. Decreasing the free-surface height by a constant of 5 m increases R_{max} by approximately 1 (figure 5). Furthermore, the runup amplification increases with increasing period, from 4 to 9+, until $P_0 = 140$, when increases are at a slower rate.

https://doi.org/10.1017/jfm.2019.618 Published online by Cambridge University Press

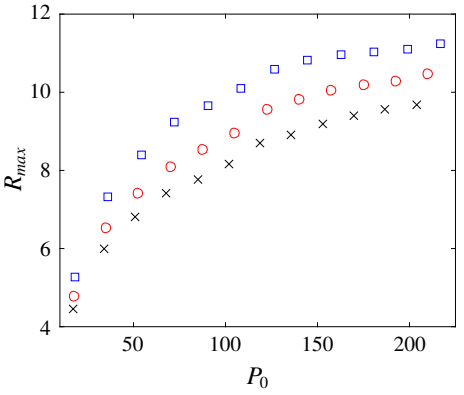


FIGURE 5. (Colour online) Maximum runup amplification R_{max} (4.1) against initial wave period P_0 for different tidal levels with the same underlying Aran Islands bathymetry (figure 2). The ocean depth is taken to be $h = 75$ m (□), 80 m (○) and 85 m (×). All wave packets are initialized dimensionally with respect to the new depths (numbers in table 1 are with respect to $h = 80$ m), and with $N_w = 3$ and $a_0 = 0.04$.

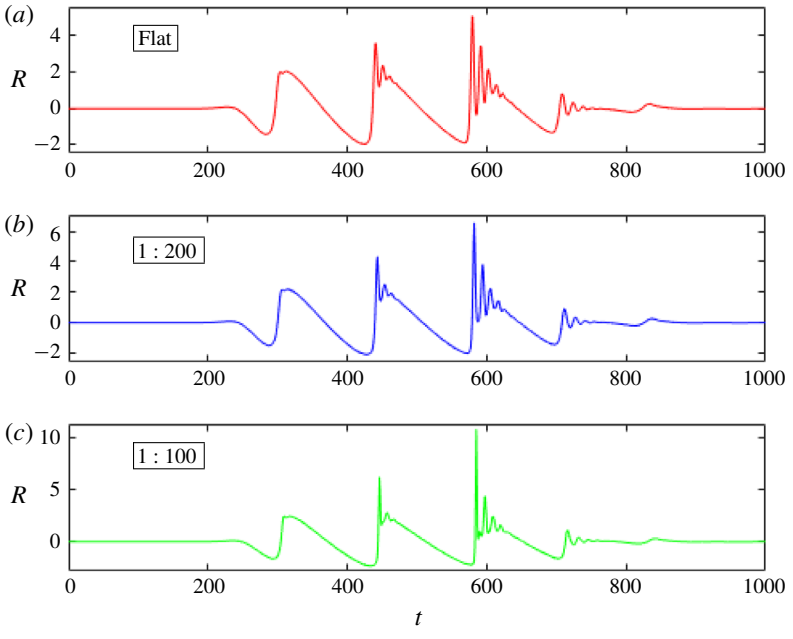


FIGURE 6. (Colour online) Runup amplification, $R(t)$, as a function of the dimensionless time t for three different bathymetries: flat, flat followed by a 1 : 200 slope, flat followed by a 1 : 100 slope. The 1 % slope represents the Aran Islands bathymetry (figure 2). In all simulations $P_0 = 140$, $N_w = 3$, $a_0 = 0.04$.

4.3.3. *Extreme waves*

As discussed, the bathymetry plays a crucial role in runup amplification of waves. In figure 6, we show the runup $R(t)$ for a wave packet with dimensionless parameters $(P_0, N_w, a_0) = (140, 3, 0.04)$ over three different bathymetries: flat, flat followed

https://doi.org/10.1017/jfm.2019.618 Published online by Cambridge University Press

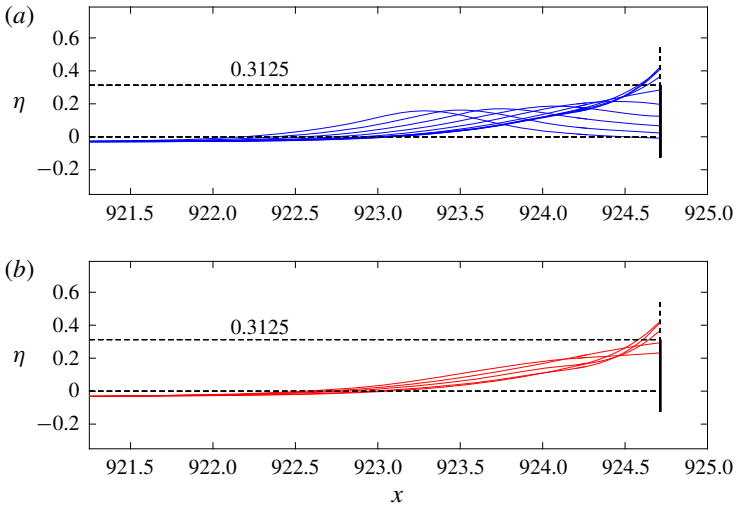


FIGURE 7. (Colour online) Runup of a wave with initial parameters $P_0 = 175$, $N_w = 3$, $a_0 = 0.043$. (*a*) The wave runs up the cliff. (*b*) The wave is reflected from the cliff. The amplification is $R_{max} \approx 11.8$. The wave smoothly runs up the face of the cliff, to the right. A cliff of (dimensionless height) 0.3125 (marked by a solid vertical line at the wall and a dashed horizontal line, dimensionally 25 m) would be overtopped by the wave.

by a 1 : 200 (0.5 %) slope, flat followed by a 1 : 100 (1 %) slope. The 1 : 100 slope represents the Aran Islands bathymetry as approximated in figure 2, with full wave simulation in Herterich & Dias (2017*a*). During each simulation, there are three significant sets of peaks (for the three crests in the initial wave packet). In each set, there is an increasing amount of wave disintegration and amplification, similar to the wave evolution in Akrish *et al.* (2016*a*,*b*). This is due to nonlinear wave–wave interactions between incoming and reflecting waves. However, allowing for the bathymetry to vary, the runup is significantly amplified from a maximum $R \approx 4.7$ in the flat case to $R \approx 10.76$ in the Aran Islands bathymetry case. Hence we clearly see an amplification increase from the wave–wave interactions and from the bathymetry slope.

We examine more closely the free surface during wave runup of one of the most amplified waves, with $P_0 = 175$, $a_0 = 0.043$ and $N_w = 3$, over the Aran Islands bathymetry. The third wave (with greatest amplification) in the wave packet smoothly runs up and down the cliff face with no sign of a vertical jet (figure 7). The crest, when it is on the cliff face, has a half-wavelength of over 1.25 (dimensionally 100 m). Here, $R_{max} \approx 11.8$. We highlight that a cliff of 25 m (marked by a solid vertical line at wall and a dashed horizontal line) would be overtopped by this wave.

We consider now the Aran Islands bathymetry (figure 2) to determine extreme waves that may occur in the near shore. We focus on the wave amplification and location when H is large, as this is directly related to large wave heights.

In all simulations, the majority of non-breaking waves during evolution respect the generally accepted condition $H < 0.55$. However, many exceed this value for small time intervals (figure 3). The maximum value is $H \approx 0.951$. Although not shown, there is a continuous $H(t)$ relationship that ascends to and descends from these (non-breaking) maximal values.

https://doi.org/10.1017/jfm.2019.618 Published online by Cambridge University Press

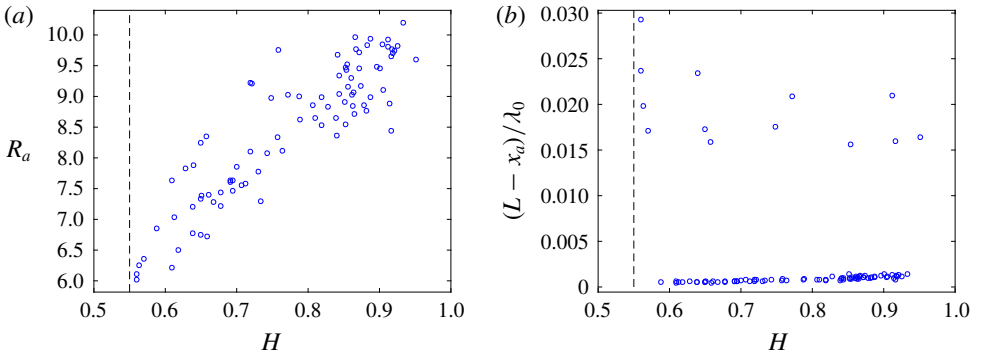


FIGURE 8. (Colour online) Amplification and location of non-breaking crests with maximum $H_w > 0.55$. (*a*) Free-surface crest amplification $R_a = \eta/a_0$. (*b*) Distance from the wall $(L - x_a)$, scaled with the initial wavelength λ_0.

Such wave events occur briefly during wave–wall and wave–wave interactions. These waves have the largest non-breaking kinematic ($K > 0.487$) and steepness ($S > 0.323$) measures. All other non-breaking waves with $H < 0.55$ have lower kinematic and steepness measures. Hence, these waves are amplified, steep and near breaking.

The scaled free-surface amplification $R_a = \eta/a_0$ at the crests tips of maximum H show that all waves are significantly amplified (figure 8*a*); $R_a > 10$ in one case and $R_a > 6$ for all. In general, R_a increases with H. The location x_a of these waves is evaluated as within $0.001\lambda_0$ of the wall for most of the waves (figure 8*b*). However, it is actually occurring on the wall face as $\approx 0.001\lambda_0$ is a small numerical error when mapping between conformal and physical space with computational domain length $2L = 100 + 2(2 + N_w)\lambda_0$. The instances further from the wall ($>0.015\lambda_0$) are wave–wave interactions between an incoming and reflected waves.

We call these amplified, steep, near-breaking waves at the wall extreme waves.

4.4. *Other bathymetry profiles*

It has been shown how a change in bathymetry slope can affect the runup amplification: the amplification, R_{max}, increases with slope (over the same x distance). In this section, we consider further the effects of bathymetry.

The different piecewise-linear profiles already mentioned are not constrained by any conservation principle to give a meaningful comparison. Now we consider profiles, $d(x)$, such that the area of the bathymetry is constant,

$$A = \int_0^L d(x)\,\mathrm{d}x = \text{const.} \tag{4.2}$$

The representation taken is a Gaussian profile,

$$d(x) = 1 - d_L \exp\left[-\left(\frac{x - L}{\sigma}\right)^2\right], \quad \sigma = \frac{2A}{\sqrt{\pi}\, d_L}, \tag{4.3a,b}$$

where d_L is the highest point of the bathymetry (at the wall, $x = L$).

https://doi.org/10.1017/jfm.2019.618 Published online by Cambridge University Press

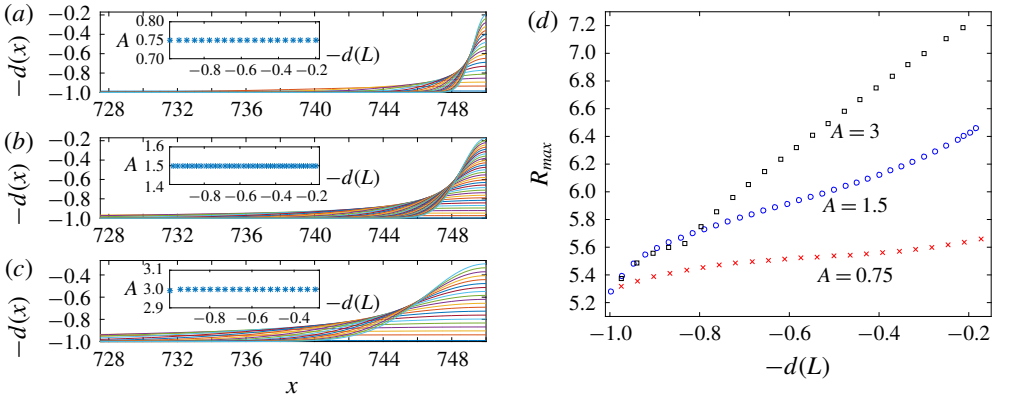


FIGURE 9. (Colour online) (*a–c*) Bathymetries based on Gaussian profiles (4.3). In each the area ($A = 0.75, 1.5, 3$ respectively) is the same but the shape differs. (*d*) The maximum runup amplification for each profile. The profiles are indicated by the bathymetry value at the wall, $-d(L)$, for different areas $A = 0.75$ (×), 1.5 (○) and 3 (□).

We initialize the wave packet in each simulation by dimensionless parameters $(P_0, N_w, a_0) = (140, 3, 0.04)$. We vary the bathymetry (4.3) via the Gaussian height (d_L) and area A. We compare three examples with $A = 0.75, 1.5, 3$, as in figures 9(*a*), 9(*b*), 9(*c*) respectively. While conserving area (4.2) under the bathymetry, the maximum runup amplification increases as the Gaussian profiles change from short and wide to tall and thin, i.e. as A increases or $d(L)$ decreases (figure 9*d*). This means that steeper bathymetry profiles have a greater amplification effect, as expected. Furthermore, as the area taken up by the bathymetry increases, meaning the waves are affected farther out to sea or with a smaller depth, the amplification increases. Eventually, as the bathymetry steepens or $d(L)$ decreases (becomes shallower), wave breaking begins to occur. There is a smaller non-breaking range as A increases.

5. Discussion and relevance to the real world

In this paper, we have discussed the appearance of near-shore extreme waves (steep, amplified, near breaking) at a vertical wall. The large amplification factors arise from the many (wave, wall, bathymetry) interactions in the system. It is natural to ask the question: Can these factors be a key element in describing cliff overtopping and boulder transport on platforms (Herterich, Cox & Dias 2018)?

The numerical values used in this paper for the incoming long waves could represent tsunamis. They could also represent infragravity waves (IGWs) or storm surges in terms of wave periods. IGWs and long storm surges are highly energetic and can magnify runup amplifications (Montoya & Lynett 2018). But the wave amplitudes and the bathymetry used in the present paper are not representative of such waves. So, at this stage, we cannot conclude that the runup amplifications described in the present paper can explain natural phenomena.

Our results can contribute to a better understanding of wave breaking in the real world. Wave breaking presents a challenge to numerical modelling. Usually the wave form cannot be resolved beyond certain limits. Furthermore, we must ensure that the breakdown is not a bug in the code, but is actually a physical process such as whitecapping (breakdown of the free surface) or overturning (multifunction). Our physical assumptions in modelling the Euler equations do not capture complex air–sea

https://doi.org/10.1017/jfm.2019.618 Published online by Cambridge University Press

interactions. Previously, the occurrence of wave breaking in this code was considered with respect to wave steepness (Viotti *et al.* 2013, 2014*a*). We justify the occurrence of wave breaking in our simulations with reference to well-regarded and well-tested criteria based on geometric, kinematic and energetic principles. Our analysis indicates that the breakdown of simulations concurs with accepted critical values (table 2). Our simulations are performed with a potential flow model. This works very well for the onset of wave breaking (Barthelemy *et al.* 2018). Beyond breaking, computational fluid dynamics (CFD) simulations are required to resolve the flow (Derakhti *et al.* 2018).

As discussed, we cannot simulate wave breaking, but can observe the wave during the onset of breaking. Let us now consider the type of breaking wave that may occur in our study. In our simulations, the breaking measures (figure 3) suggest steep waves with crest tip velocities that exceed the phase velocity. On occasions, waves are considered excessive for only one of the measures. This suggests either plunging or spilling as the typical breaking wave type. Larger steepness, kinematic, energetic and breaking strength measures are associated with plunging (Perlin *et al.* 2013; Derakhti *et al.* 2018). The breaking strength of waves is related to the rate of change of normalized energy flux (2.14). Waves initialized with high amplitudes have the greatest breaking strengths (figure 4*b*).

The influence of the bathymetry is explored with a few examples. Specifically, a representation of the Aran Islands, Ireland is considered, along with variations thereof. Tidal differences highlight the effect of depth and bathymetry variation. While a varying bathymetry affects runup amplification, it further depends on the absolute depth that governs the system. Low tides, while possessing a lower still-water free-surface elevation, are amplified by a greater amount than high tides, which possess a higher still-water level (figure 5).

Gaussian bathymetries are compared with respect to the area under the curve (figure 9). However, there are many other representative bathymetries not considered here. We can say that steepness, height, total area (displacement) of a bathymetry all contribute to increasing the runup amplification, as well as the absolute depth from the tidal effect. The bathymetry increases the runup not just far beyond linear theory, but also nonlinear results over a flat bottom.

Wave–wave interactions, a result of reflection from the wall, are key in our results and clearly affect the criteria for wave breaking. Waves are amplified by interactions with other waves in the group (figure 6), reducing the initial amplitude range for non-breaking waves (figure 3*b* in Herterich & Dias (2017*a*)).

6. Conclusions

The runup of long waves at a wall can be significantly amplified by a variable bathymetry, wave–wall interactions and wave–wave interactions (figure 6), under the influence of dispersion and nonlinearity. Wave breaking is a prominent feature with a slope representing the Aran Islands bathymetry (figure 2). In particular, the nonlinear interactions of multiple waves in the wave packet reduce the maximum initial amplitude range before breaking occurs from 0.063 to 0.043 (dimensionally, 5.04 m to 3.44 m).

Wave breaking is verified with respect to several well-established criteria. The geometric (2.8), (2.9), kinematic (2.10) and energetic (2.15) breaking measures are applied to the free-surface crests in the simulations. In general there is a well-defined separation between breaking and non-breaking waves. However, there are some

https://doi.org/10.1017/jfm.2019.618 Published online by Cambridge University Press

inconsistencies (overlapping) where non-breaking waves take breaking measures that exceed the breaking waves (figure 3). For the parameter regime in table 1, the criteria are summarized in table 2. The minimum breaking criteria obtained ($S = 0.364$, $H = 0.452$, $K = 0.697$ and $B = 0.871$) are reasonably consistent for the geometric measures, and consistent for the kinematic and energetic measures (Stansell & MacFarlane 2002; Wu & Nepf 2002; Perlin *et al.* 2013; Barthelemy *et al.* 2018).

The initial amplitude and period may influence the type of breaking. Shorter-period and higher-amplitude wave packets result in steeper waves, with larger kinematic breaking measures and breaking strengths. These are more likely to be plunging-type breaking waves, with longer periods and smaller amplitudes likely to be spilling-type breaking (Perlin *et al.* 2013; Derakhti *et al.* 2018).

For non-breaking waves, the maximum runup amplification increases with many parameters: initial amplitude, number of waves, N_w, in the wave packet (until $N_w \geqslant 3$ where it steadies out), tidal level and slope of bathymetry (figure 5). However, the runup increases with dimensionless wave periods until up to 140, from an amplification factor of 4 to 9+ (figure 5). Beyond this period, the runup continues to increase but at a lower rate. The wave smoothly runs up the wall without exhibiting a flip-through like jet (figure 7).

Tidal effects change the depth of the bathymetry by a constant change in free-surface elevation. We investigate 5 m changes in the still-water level. The runup amplification reduces by 1 with each 5 m increment (figure 5). This means that a greater depth reduces the runup amplification. The bathymetric effect is reduced with depth.

The non-breaking waves with excessive geometric and kinematic breaking measures are analysed with respect to extreme wave height-to-depth ratios. It is observed that these waves are steep, near breaking, close to the wall, with an amplification factor of 6–10.76 (figure 8). We refer to these waves as extreme near-shore waves. They smoothly run up a wall to great heights, such that they may overtop with a collapsing surge if the wall is of finite height.

Variations in bathymetry are also explored using Gaussian distributions (4.3), keeping a constant area under the profile. The runup amplification increases as the profile becomes steeper over a shorter range (figure 9). Furthermore, runup amplification increases with the area under the bathymetry curve. This is as one may expect with the bathymetry becoming a more prominent feature of the system.

The extreme amplifications obtained in this paper are for wave periods that are not typical of ocean waves. However, they can be reproduced in laboratory experiments.

Acknowledgements

Preliminary results were given in two conference papers (Herterich & Dias 2017*a*,*b*) with several results included as appeared, extended or corrected. The authors thank Geological Survey Ireland and the Marine Institute for providing access to the INSS and INFOMAR datasets, and C. Viotti for his original conformal-mapping code for the Euler equations. J.G.H. would like to thank J. Brennan for helpful discussions during the preparation of this manuscript. This study was funded by Science Foundation Ireland (SFI) under the research project 'Understanding Extreme Nearshore Wave Events through Studies of Coastal Boulder Transport' (14/US/E3111).

REFERENCES

AKRISH, G., RABINOVITCH, O. & AGNON, Y. 2016*a* Extreme run-up events on a vertical wall due to nonlinear evolution of incident wave groups. *J. Fluid Mech.* **797**, 644–664.

https://doi.org/10.1017/jfm.2019.618 Published online by Cambridge University Press

AKRISH, G., SCHWARTZ, R., RABINOVITCH, O. & AGNON, Y. 2016*b* Impact of extreme waves on a vertical wall. *Nat. Hazards* **84** (2), 637–653.

BABANIN, A. V., CHALIKOV, D., YOUNG, I. R. & SAVELYEV, I. 2010 Numerical and laboratory investigation of breaking of steep two-dimensional waves in deep water. *J. Fluid Mech.* **644**, 433–463.

BANNER, M. L., BARTHELEMY, X., FEDELE, F., ALLIS, M., BENETAZZO, A., DIAS, F. & PEIRSON, W. L. 2014 Linking reduced breaking crest speeds to unsteady nonlinear water wave group behavior. *Phys. Rev. Lett.* **112** (11), 114502.

BARTHELEMY, X., BANNER, M. L., PEIRSON, W. L., FEDELE, F., ALLIS, M. & DIAS, F. 2018 On a unified breaking onset threshold for gravity waves in deep and intermediate depth water. *J. Fluid Mech.* **841**, 463–488.

BENOIT, M., DIAS, F., HERTERICH, J. G. & SCOLAN, Y.-M. 2018 A discriminating test-case for the simulation of the propagation and run-up of tsunami-type wave trains. In *16th Journées de l'Hydrodynamique, Marseille, 27–29 November 2018*; http://website.ec-nantes.fr/actesjh/images/16JH/16JH-actes.htm.

BOLLES, C. T., SPEER, K. & MOORE, M. N. J. 2019 Anomalous wave statistics induced by abrupt depth change. *Phys. Rev. Fluids* **4** (1), 011801.

BRENNAN, J., CLANCY, C., HARRINGTON, J., COX, R. & DIAS, F. 2017 Analysis of the pressure at a vertical barrier due to extreme wave run-up over variable bathymetry. *Theor. Appl. Mech. Lett.* **7** (5), 269–275.

BRENNAN, J., VIOTTI, C. & DIAS, F. 2014 Pressure fluctuations on a vertical wall during extreme run-up cycles. In *ASME 2014 33rd International Conference on Ocean, Offshore and Arctic Engineering*, p. V04AT02A038. American Society of Mechanical Engineers.

BRÜHL, M. & OUMERACI, H. 2016 Analysis of long-period cosine-wave dispersion in very shallow water using nonlinear Fourier transform based on KdV equation. *Appl. Ocean Res.* **61**, 81–91.

CARBONE, F., DUTYKH, D., DUDLEY, J. M. & DIAS, F. 2013 Extreme wave runup on a vertical cliff. *Geophys. Res. Lett.* **40** (12), 3138–3143.

CHAMBAREL, J., KHARIF, C. & TOUBOUL, J. 2009 Head-on collision of two solitary waves and residual falling jet formation. *Nonlinear Process. Geophys.* **16**, 111–122.

CHEN, Y. Y., KHARIF, C., YANG, J. H., HSU, H. C., TOUBOUL, J. & CHAMBAREL, J. 2015 An experimental study of steep solitary wave reflection at a vertical wall. *Eur. J. Mech. (*B*/Fluids)* **49**, 20–28.

CHOI, W. & CAMASSA, R. 1999 Exact evolution equations for surface waves. *J. Engng Mech.* **125** (7), 756–760.

COOKER, M. J. & PEREGRINE, D. H. 1995 Pressure-impulse theory for liquid impact problems. *J. Fluid Mech.* **297**, 193–214.

CRAIG, W. 2006 Surface water waves and tsunamis. *J. Dyn. Differ. Equ.* **18** (3), 525–549.

CYRIL, J. & GALVIN, C. J. 1972 Wave breaking in shallow water. In *Waves on Beaches and Resulting Sediment Transport*, pp. 413–456. Elsevier.

DERAKHTI, M., BANNER, M. L. & KIRBY, J. T. 2018 Predicting the breaking strength of gravity water waves in deep and intermediate depth. *J. Fluid Mech.* **848**, R2 1–11.

DIAS, F. & GHIDAGLIA, J. M. 2018 Slamming: recent progress in the evaluation of impact pressures. *Annu. Rev. Fluid Mech.* **50**, 243–273.

DRAZEN, D. A., MELVILLE, W. K. & LENAIN, L. 2008 Inertial scaling of dissipation in unsteady breaking waves. *J. Fluid Mech.* **611**, 307–332.

DUNCAN, J. H. 1983 The breaking and non-breaking wave resistance of a two-dimensional hydrofoil. *J. Fluid Mech.* **126**, 507–520.

FEDELE, F. 2014 Geometric phases of water waves. *Europhys. Lett.* **107** (6), 69001.

GEOLOGICAL SURVEY IRELAND 2002–2016 INSS and INFOMAR bathymetry mapping. http://maps.marine.ie/infomar/, online; accessed 2016-04-18.

GODA, Y. 1975 New wave pressure formulae for composite breakwaters. In *Coastal Engineering 1974*, pp. 1702–1720. American Society of Civil Engineers.

GODA, Y. 2010 Reanalysis of regular and random breaking wave statistics. *Coast. Engng J.* **52** (01), 71–106.

https://doi.org/10.1017/jfm.2019.618 Published online by Cambridge University Press

GRILLI, S. T., SVENDSEN, I. A. & SUBRAMANYA, R. 1997 Breaking criterion and characteristics for solitary waves on slopes. *J. Waterway, Port Coast. Ocean Engng* **123** (3), 102–112.

GRUE, J. & KOLAAS, J. 2017 Experimental particle paths and drift velocity in steep waves at finite water depth. *J. Fluid Mech.* **810**, R1 1–10.

GRUE, J., KOLAAS, J. & JENSEN, A. 2014 Velocity fields in breaking-limited waves on finite depth. *Eur. J. Mech. (*B*/Fluids)* **47**, 97–107.

HANSOM, J. D., BARLTROP, N. D. P. & HALL, A. M. 2008 Modelling the processes of cliff-top erosion and deposition under extreme storm waves. *Mar. Geol.* **253** (1), 36–50.

HERTERICH, J. G., COX, R. & DIAS, F. 2018 How does wave impact generate large boulders? Modelling hydraulic fracture of cliffs and shore platforms. *Mar. Geol.* **399**, 34–46.

HERTERICH, J. G. & DIAS, F. 2017*a* Wave breaking and runup of long waves approaching a cliff over a variable bathymetry. *Proc. IUTAM* **25**, 18–27.

HERTERICH, J. G. & DIAS, F. 2017*b* Wave height to depth measures during extreme runup. In *The 27th International Ocean and Polar Engineering Conference*, vol. 3, pp. 1390–1394. International Society of Offshore and Polar Engineers.

HWANG, P. A., XU, D. & WU, J. 1989 Breaking of wind-generated waves: measurements and characteristics. *J. Fluid Mech.* **202**, 177–200.

IAFRATI, A., DE VITA, F. & VERZICCO, R. 2019 Effects of the wind on the breaking of modulated wave trains. *Eur. J. Mech. (*B*/Fluids)* **73**, 6–23.

KURNIA, R. & VAN GROESEN, E. 2014 High order Hamiltonian water wave models with wave-breaking mechanism. *Coast. Engng* **93**, 55–70.

KURNIA, R. & VAN GROESEN, E. 2017 Localization for spatial–spectral implementations of 1D analytic Boussinesq equations. *Wave Motion* **72**, 113–132.

LONGO, S., CLAVERO, M., CHIAPPONI, L. & LOSADA, M. A. 2017 Invariants of turbulence Reynolds stress and of dissipation tensors in regular breaking waves. *Water* **9** (11), w9110893.

LUGNI, C., BROCCHINI, M. & FALTINSEN, O. M. 2006 Wave impact loads: the role of the flip-through. *Phys. Fluids* **18** (12), 122101.

MADER, C. L. 1974 Numerical simulation of tsunamis. *J. Phys. Oceanogr.* **4** (1), 74–82.

MADSEN, P. A. & FUHRMAN, D. R. 2008 Run-up of tsunamis and long waves in terms of surf-similarity. *Coast. Engng* **55** (3), 209–223.

MADSEN, P. A., FUHRMAN, D. R. & SCHÄFFER, H. A. 2008 On the solitary wave paradigm for tsunamis. *J. Geophys. Res.* **113** (C12), C12012.

MASSEL, S. R. 1996 On the largest wave height in water of constant depth. *Ocean Engng* **23** (7), 553–573.

MAYER, R. H. & KRIEBEL, D. L. 1995 Wave runup on composite-slope and concave beaches. In *Coastal Engineering 1994*, pp. 2325–2339. American Society of Civil Engineers.

MEI, C. C., STIASSNIE, M. & YUE, D. K.-P. 1989 *Theory and Applications of Ocean Surface Waves: Part 1: Linear Aspects. Part 2: Nonlinear Aspects*. World Scientific.

MELVILLE, W. K. 1996 The role of surface-wave breaking in air–sea interaction. *Annu. Rev. Fluid Mech.* **28** (1), 279–321.

MONTOYA, L. & LYNETT, P. 2018 Tsunami versus infragravity surge: comparison of the physical character of extreme runup. *Geophys. Res. Lett.* **45** (23), 12–982.

MUNK, W. H. 1949 The solitary wave theory and its application to surf problems. *Ann. N.Y. Acad. Sci.* **51** (3), 376–424.

NELSON, R. C. 1994 Depth limited design wave heights in very flat regions. *Coast. Engng* **23** (1–2), 43–59.

NING, D., LI, X. & ZHANG, C. 2018 Nonlinear simulation of wave train impact on a vertical seawall. *Water* **10** (8), 986.

PEREGRINE, D. H. 2003 Water–wave impact on walls. *Annu. Rev. Fluid Mech.* **35** (1), 23–43.

PERLIN, M., CHOI, W. & TIAN, Z. 2013 Breaking waves in deep and intermediate waters. *Annu. Rev. Fluid Mech.* **45**, 115–145.

PHILLIPS, O. M. 1985 Spectral and statistical properties of the equilibrium range in wind-generated gravity waves. *J. Fluid Mech.* **156**, 505–531.

https://doi.org/10.1017/jfm.2019.618 Published online by Cambridge University Press

RIEDEL, H. P. & BYRNE, A. P. 1987 Random breaking waves – horizontal seabed. In *Coastal Engineering 1986*, pp. 903–908. American Society of Civil Engineers.

RYU, Y. & CHANG, K.-A. 2008 Green water void fraction due to breaking wave impinging and overtopping. *Exp. Fluids* **45** (5), 883–898.

RYU, Y., CHANG, K.-A. & MERCIER, R. 2007 Runup and green water velocities due to breaking wave impinging and overtopping. *Exp. Fluids* **43** (4), 555–567.

SAKET, A., PEIRSON, W. L., BANNER, M. L. & ALLIS, M. J. 2018 On the influence of wave breaking on the height limits of two-dimensional wave groups propagating in uniform intermediate depth water. *Coast. Engng* **133**, 159–165.

SAKET, A., PEIRSON, W. L., BANNER, M. L., BARTHELEMY, X. & ALLIS, M. J. 2017 On the threshold for wave breaking of two-dimensional deep water wave groups in the absence and presence of wind. *J. Fluid Mech.* **811**, 642–658.

SAVILLE, T. JR 1957 Wave run-up on composite slopes. *Coast. Engng Proc.* **1** (6), 41.

SCHWENDEMAN, M. S. & THOMSON, J. 2017 Sharp-crested breaking surface waves observed from a ship-based stereo video system. *J. Phys. Oceanogr.* **47** (4), 775–792.

SEIFFERT, B. R. & DUCROZET, G. 2018 Simulation of breaking waves using the high-order spectral method with laboratory experiments: wave-breaking energy dissipation. *Ocean Dyn.* **68**, 65–89.

SEIFFERT, B. R., DUCROZET, G. & BONNEFOY, F. 2017 Simulation of breaking waves using the high-order spectral method with laboratory experiments: wave-breaking onset. *Ocean Model.* **119**, 94–104.

STANSELL, P. & MACFARLANE, C. 2002 Experimental investigation of wave breaking criteria based on wave phase speeds. *J. Phys. Oceanogr.* **32** (5), 1269–1283.

TOFFOLI, A., BABANIN, A., ONORATO, M. & WASEDA, T. 2010 Maximum steepness of oceanic waves: field and laboratory experiments. *Geophys. Res. Lett.* **37** (5), L05603.

TRILLO, S., DENG, G., BIONDINI, G., KLEIN, M., CLAUSS, G. F., CHABCHOUB, A. & ONORATO, M. 2016 Experimental observation and theoretical description of multisoliton fission in shallow water. *Phys. Rev. Lett.* **117** (14), 144102.

VIOTTI, C., CARBONE, F. & DIAS, F. 2014 Conditions for extreme wave runup on a vertical barrier by nonlinear dispersion. *J. Fluid Mech.* **748**, 768–788.

VIOTTI, C. & DIAS, F. 2014 Extreme waves induced by strong depth transitions: fully nonlinear results. *Phys. Fluids* **26** (5), 051705.

VIOTTI, C., DUTYKH, D. & DIAS, F. 2014 The conformal-mapping method for surface gravity waves in the presence of variable bathymetry and mean current. *Proc. IUTAM* **11**, 110–118.

VIOTTI, C., DUTYKH, D., DUDLEY, J. M. & DIAS, F. 2013 Emergence of coherent wave groups in deep-water random sea. *Phys. Rev.* E **87** (6), 063001.

WEGGEL, J. R. 1973 Maximum breaker height for design. In *Coastal Engineering 1972*, pp. 419–432.

WU, C. H. & NEPF, H. M. 2002 Breaking criteria and energy losses for three-dimensional wave breaking. *J. Geophys. Res.* **107** (C10), 3177.

WU, Y. H. & TIAN, J.-W. 2000 Mathematical analysis of long-wave breaking on open channels with bottom friction. *Ocean Engng* **27** (2), 187–201.

XU, D., HWANG, P. A. & WU, J. 1986 Breaking of wind-generated waves. *J. Phys. Oceanogr.* **16** (12), 2172–2178.

https://doi.org/10.1017/jfm.2019.618 Published online by Cambridge University Press